Scientific Reports

https://doi.org/10.1038/s41598-026-42847-8

Article in Press

Deep learning–based basilar artery wall and lumen segmentation from 1-mm MR vessel wall imaging

Received: 7 November 2025

Accepted: 27 February 2026

Published online: 03 March 2026

Cite this article as: Tsou C., Liu H. & Huang A. Deep learning–based basilar artery wall and lumen segmentation from 1-mm MR vessel wall imaging. *Sci Rep* (2026). https://doi.org/10.1038/s41598-026-42847-8

Chien-Hung Tsou, Hon-Man Liu & Adam Huang

Deep Learning–Based Basilar Artery Wall and Lumen Segmentation from 1-mm MR Vessel Wall Imaging

Chien-Hung Tsou[1], Hon-Man Liu[2]*, Adam Huang[1]*

[1]Department of Biomedical Sciences and Engineering, National Central University, Zhongli, Taiwan
[2]Department of Medical Imaging, Fu Jen Catholic University Hospital, Fu Jen Catholic University, New Taipei City, Taiwan

*Corresponding Authors:
Adam Huang, Ph.D.
Department of Biomedical Sciences and Engineering
National Central University, Taoyuan City 320317, Taiwan
Email: adamhuan@ncu.edu.tw; adamhuan@gmail.com
Phone: +886-3-4227151 ext. 27722
Fax: +886-3-4226062

Hon-Man Liu, MD
Department of Radiology
Fu Jen Catholic University Hospital, Fu Jen Catholic University,
No. 69, Guizi Road, Taishan District, New Taipei City 24352, Taiwan (R.O.C.)
Email: inr.liu@gmail.com
Phone: +886-2-8512-8888
Fax: +886-2-8512-8897
Drs Huang and Liu share equal correspondence responsibility

Abstract

Background To investigate the morphology of the basilar artery (BA) using 1-mm magnetic resonance (MR) vessel wall imaging (VWI).

Methods This retrospective study included 36 patients who underwent intracranial 1-mm MR-VWI. The BA morphology was evaluated following a machine learning paradigm. Twenty patients (1073 cross-sectional BA images) were used to fine-tune a pre-trained deep learning model, Mask-RCNN, for BA segmentation. Six (373 cross-sectional BA images) were used for model validation and 10 (186 axial BA images) for comparison with human expert ratings. Human expert ratings were conducted in radial directions oriented at 3, 6, 9, and 12 o'clock. Agreement between human expert and machine estimation was evaluated using the intraclass correlation coefficient (ICC) and statistical significance was estimated by paired student's t-test. BA wall segmentation was assessed using the intersection-over-union (IOU) metric.

Results The BA exhibits a tapered shape, with the widest diameter at the beginning (3.17 ± 0.69 mm) and significantly narrowing towards the end (2.71 ± 0.55 mm) (p-value<0.001). The deep-learning model demonstrated moderate to excellent agreement with human expert ratings (ICC: 0.72-0.83) when measuring BA

diameter. However, agreement was less optimal (ICC<0.5) when measuring artery wall thickness. For vessel wall segmentation, the model achieved a mean IOU score of 0.756 ± 0.079.

Conclusion This study demonstrates the effectiveness of using a 1-mm MR-VWI protocol for characterizing and evaluating the vertebrobasilar circulation. This enhanced knowledge of basilar artery shape is critical and should help neurosurgeons safely diagnose and manage posterior circulation diseases.

Keywords: Atherosclerosis, deep learning, intracranial artery, magnetic resonance angiography, vessel wall segmentation

Introduction

Approximately 20% of all transient ischaemic attacks and ischaemic strokes occur in the area of vertebrobasilar (also known as posterior) circulation [1]. Posterior circulation ischaemic stroke is complex and difficult to diagnose because patients present with a wide range of symptoms. Furthermore, the vertebrobasilar vessels and their walls are not easily evaluated by ultrasound and are only indirectly assessed by digital subtraction angiography (DSA) or conventional magnetic resonance (MR) techniques [2,3]. The basilar artery (BA) is the main conduit that supplies oxygen-rich blood to the posterior cerebral circulation. Atherosclerosis in the BA can limit or block blood flow to the cerebellum, brainstem, thalamus, occipital, and temporal lobes [4].

Diagnosis of BA stenosis is challenging as the morphology of the BA varies according to aging and vertebral artery dominance [5]. The length of BA is approximately 25–35 mm with a diameter of 2.7–4.3 mm at the proximal portion [6] and a wall thickness of 0.2–0.3 mm [7]. Both abnormal BA dilation and narrowing increase the risk of strokes. For example, a BA diameter larger than 4.3 mm suggests dolichoectasia and increases the chance of suffering a fatal stroke [8]. Conversely, a luminal diameter of 2 mm or smaller has been more commonly

observed in individuals with posterior circulation ischaemic stroke [1]. However, anatomical variability of the vertebrobasilar circulation, including BA fenestrations [9], variable fusion levels of the vertebral arteries [10], and fetal-type posterior cerebral arteries [11], can significantly alter BA geometry. Consequently, a relatively thin BA does not necessarily indicate pathology, and prominent vessels are not synonymous with dolichoectasia [11,12].

Digital subtraction angiography (DSA) is considered the gold standard for the diagnosis of BA stenosis. However, DSA is invasive and cannot detect wall thickness. Alternatively, ultrasound can identify both stenosis and wall thickness in the carotid arteries, but it is not sensitive enough to diagnose BA stenosis [13]. Due to the small diameter of BA, traditional computed tomography angiography (CTA) and magnetic resonance angiography (MRA) have limited spatial resolution or tissue contrast to accurately assess the vessel wall [14,15]. Importantly, aside from histopathologic examination or autopsy, no true gold standard exists for BA vessel wall imaging. This lack of a definitive reference standard highlights the need to investigate alternative imaging techniques that can delineate the BA vessel wall.

In recent years, magnetic resonance (MR) vessel wall imaging (VWI) has emerged as a promising noninvasive imaging modality that can directly visualize

the intracranial vessel wall and characterize plaque features with excellent soft-tissue contrast [16-18]. With its superior soft tissue contrast and spatial resolution, the MR-VWI scanning protocol allows for the direct visualization of the vessel wall and enables the differentiation of various intracranial vascular lesions [16,17]. However, measuring the vessel wall thickness and the luminal diameter of the BA is laborious and prone to the human operator variance. To enhance the efficiency and consistency of vascular morphology measurement, several deep learning models have been proposed to process CTA and MRA datasets. However, these solutions have primarily focused on segmenting the carotid artery lumen [19-22]. While more recent 3D models, such as nnU-Net [23] and TotalSegmentator [24], can perform arterial wall segmentation directly on volumetric data, they are currently limited to large vessels, such as aorta [25]. To the best of our knowledge, no deep learning models have been specifically developed for segmenting the BA due to its inherently small size and complex surrounding anatomy.

In this study, we proposed applying 2D segmentation models to cross-sectional images of the BA, resampled along the arterial centerline. This unique approach was designed to achieve high accuracy in detecting and segmenting the BA's thin wall structures. The model's accuracy was subsequently assessed by directly

comparing the machine-generated results to those provided by a human expert.

Materials and methods

This feasibility study retrospectively investigated the accuracy of deep learning models in identifying BA wall thickness and luminal diameters using a 1-mm MR-VWI scanning protocol. This study protocol was reviewed and approved by the Institutional Review Board (IRB) of Fu Jen Catholic University Hospital, Taiwan (approval no. FJUH109080). All procedures were conducted in accordance with the Declaration of Helsinki, and written informed consent was obtained from all participants.

Dataset

This retrospective, single-center study enrolled patients at Fu Jen Catholic University Hospital. A total of 38 patients who underwent MR vessel wall imaging (MR-VWI) for atherosclerosis diagnosis between November 2020 and July 2022 were included (Fig 1). Two patients were excluded due to suboptimal image quality; specifically, partial segments in these cases exhibited significant adjacency to the pons, which precluded clear visualization of the outer wall and resulted in low confidence during manual labeling. The final dataset therefore included 36 patients (28 males, mean age 63.3 ± 6.6 years; 8 females, mean age 64.0 ± 10.8 years). Each

dataset consisted of 155 slices (1 mm slice thickness, spatial resolution = 0.2246 or 0.5188 mm) acquired from the base of the pons to the top of head, encompassing vascular segments such as intracranial carotid artery, middle cerebral artery, intracranial vertebral artery, and basilar artery. Intracranial vessel wall images were acquired on a 3-Tesla MR system with BB-HR-VWI 3D variable refocusing flip angle sequence (Ingenia; Philips Healthcare, Best, the Netherlands) with the following parameters: TR/TE = 600/29.819 ms; flip angle = 90; accelerate factor = 1.0; matrix = 272×272; field of view = 230×230; slice thickness = 1 mm; spacing = 1 mm; percent phase field of view = 79%; and pixel bandwidth = 266 Hz/pixel. Our data pool of 36 study datasets includes 20 (55.5%) training and 6 (16.7%) validation datasets with their manual annotations from our previous study [26]. Ten (27.8%) datasets were reserved for testing and comparison with visual assessment by radiologists.

Preprocessing

The lumen center points of the BA (Figs. 2A and 2B) were manually selected using in-house software (implemented in MATLAB) where users only needed to select pixels by mouse clicking. These center points were interpolated to generate a smooth centerline, and cross-sectional images were resampled along the centerline

at 0.5 mm intervals with a spatial resolution of 0.1 mm (Fig 2C). The cross-sectional images, sized 160×160 pixels (16×16 mm), were rearranged in a grid with 5 rows, progressing from proximal to distal (Fig 2D). These 2D cross-sectional slices were semi-automatically annotated, as delineated in the following section.

Semi-automatic vessel wall annotation

The BA typically runs within the central groove of the pons, located in the pontine cistern. Under normal circumstances, a small gap exists between the artery and the pons to prevent compression of neural structures. This gap generally positions the BA a few millimeters anterior to the pons. However, this distance can vary individually due to factors such as BA tortuosity, atherosclerosis, or underlying pathologies like aneurysms or dolichoectasia. When the BA is in close proximity to the pons, tissue contrast in imaging can become poor, even with high-resolution MRI. This occurs because the signal intensity of the tissue between the pons and the basilar artery wall is very similar, making it challenging to distinguish between them.

Due to the aforementioned challenge, significant discrepancies emerged between automated and visual identification of the BA's outer wall near the pons; therefore, we opted to manually delineate and label the outer wall boundaries

through visual inspection. A MATLAB labeling tool (called Image Labeler App) was used to manually demarcate the BA's outer wall in the resampled 2D serial cross-sectional slices. The objective was to deduce the edge according to human visual perception along the vessel's contour (the dashed line shown in Fig 3C). The manual outer wall marking and the image itself were then processed fully automatically by using a 1D piecewise linear model (PLM) [26,27] to derive the inner wall boundaries (the dotted line shown in Fig 3D). We assumed that the inner wall border was located at the mid intensity value between the lumen intensity C_0 and the peak wall intensity Y_{max} (Fig 3C). The software drew radial samples in equally divided directions and fit the 1D intensity signal using the PLM defined in Equation (1):

$$Y = PLM(x) = \begin{cases} C_0 & 0 \le x \le x_0 \\ C_0 + C_1(x - x_0) & x_0 < x \le x_1 \end{cases} \quad (1)$$

The PLM model consists of a constant value C_0 within lumen ($0 \le x \le x_0$) and a linear model along the vessel wall from x_0 to x_1 ($x_0 \le x \le x_1$, where x_1 corresponds to the maximum value $Y(x_1) = Y_{max}$). C_0, C_1, and x_0 can be solved by minimizing the sum of squared errors (SSE):

$$SSE(C_0,C_1,x_0) = \sum_{x=0}^{x_1} (PLM(x) - y_i)^2 \quad (2)$$

Replacing the right side of Equation (1) with $C_0 + C_1 x$, where $x = 0$ if $0 \le x < x_0$, and $x = x - x_0$ if $x_0 < x \le x_1$, Equation (1) can be simplified as:

$$PLM(x) = C_0 + C_1 \times x \quad (3)$$

The parameters C_0 and C_1 in Equation (3) can be efficiently solved through linear least-squares estimation. Consequently, x_0 can be found using linear search to minimize Equation (2). Lastly, the inner wall is located at mid intensity, $(C_0 + Y_{max})/2$, by linearly searching between x_0 and x_1.

Model training and validation

We fine-tuned a pre-trained model, Detection2, which was originated from the Mask RCNN framework proposed by Facebook Artificial Intelligence Research (FAIR) [28], to detect and segment the BA's wall as a ring-shaped object (Fig 3E) by transfer learning. From the 20 subjects in the training group, 1073 BA cross-sectional images, sized 160×160 pixels (0.1 mm/pixel), with their respective BA wall semantic segmentation annotation files were collected as the training dataset. The annotation files were then converted to the COCO dataset format [29]. Our experiment was conducted on the Google Colaboratory platform using the PyTorch model provided in the official FAIR Detectron2 tutorial and documentation. We selected MASK-RCNN-R50-FPN-3X as the backbone and fine-tuned the Detectron2 model with a learning rate of 0.0025 and a maximum iteration limit of 3000. The trained model was configured with an object detection threshold of 0.7 and a

maximum of 120 objects detected per image.

For model validation, the segmentation performance was evaluated based on overlap, using the intersection over union (IOU) score with 373 BA cross-sectional images from the 6 subjects in the test group. IOU score is defined as:

$$\text{IOU} = \frac{\text{Area of Overlap}}{\text{Area of Union}}.$$

Visual performance comparison

To assess the level of agreement between AI models and human experts, 10 additional hold-out datasets (comprising 186 axial view images) were used to measure BA wall and lumen. These datasets were not included in the training and validation phases of the AI development process. The measurements were taken following a specific visual examination protocol [30]. This protocol involved sampling measurements at four key positions: 12 o'clock (anterior), 3 o'clock, 6 o'clock, and 9 o'clock. A neuroradiologist (H.M.L. with over 30 years of experience) measured the transverse diameter (Trans), anteroposterior diameter (AP), luminal transverse diameter (LTrans), luminal anteroposterior diameter (LAP), wall thickness at 9 o’clock (RTrans), and wall thickness at 12 o’clock (AAP) (illustrated in Fig. 4). The visual measurements were performed on the original axial view DICOM images, all of which were magnified 801.75 times for visual estimation using MicroDicom

Viewer (MicroDicom, Sofia, Bulgaria). For AI models, the test images were also cropped from the original axial view DICOM images and resized to 160×160 pixels with a spatial resolution of 0.1 mm/pixel.

Luminal diameter definition

Mean luminal diameter was defined as the mean value of LAP and LTrans (Fig 4A):

$$D\ (x = i) = \frac{LAP(x=i) + LTrans(x=i)}{2}$$

where $x = i$ represented the i-th cross-sectional resampling image from BA's proximal end (Fig 2D). In addition, three sectional BA luminal diameters were defined at the proximal, mid, and distal segments as:

$$D_{prox} = \frac{3}{N}\sum_{i=1}^{\frac{N}{3}} D(x = i),$$

$$D_{mid} = \frac{3}{N}\sum_{i=\frac{N}{3}+1}^{\frac{2N}{3}} D(x = i),$$

$$D_{dist} = \frac{3}{N}\sum_{i=\frac{2N}{3}+1}^{N} D(x = i).$$

where N was the total number of resampling images, and D_{prox}, D_{mid}, D_{dist} stood for proximal, mid, and distal BA diameters respectively.

Statistical analysis

Intraclass correlation coefficient (ICC, two-way mixed model for absolute agreement, single measurement) was used to assess the degree of agreement for the six BA morphological (Trans, AP, Ltrans, LAP, RTrans, and AAP) measurements

between the trained AI model and the radiologist expert. The ICC analysis was also used to assess the agreement between the trained AI model and the PLM method. The 95% confidence intervals (CI) of the estimated ICC scores were calculated from 10,000 bootstrap simulations. An ICC score less than 0.5 indicates poor reliability, between 0.5 and 0.75 moderate reliability, between 0.75 and 0.9 good reliability, and greater than 0.9 excellent reliability [31]. Student's t-test was used to determine statistical significance in the mean differences of D_{prox}, D_{mid}, and D_{dist}.

Results

BA wall detection and segmentation

The fine-tuned Detectron2 model successfully detected and segmented BA arterial walls from 371 (99.5%) out of 373 cross-sectional images from the 6 test datasets with a mean IOU score of 0.756 ± 0.079 mm. Figure 5 illustrates some examples of segmented ring-shaped BA walls. The trained model successfully detected all arterial walls for both the images with good conspicuity (left) and those with fair conspicuity (right). The model's less accurate outer wall segmentations were mainly due to small vessels, such as pontine arteries, branching out of the BA (indicated by the arrow in Figure 5).

Morphological measurements and ICC reliability analysis

In processing the 10 hold-out datasets for visual measurement comparison, the fine-tuned Detectron2 model successfully detected and segmented BA arterial walls from 183 (98.4%) out of 186 axial view images. Of the 183 segmented arterial walls, BA morphological measurements of AP, Trans, AAP, RTrans, LAP, and LTrans were 4.963 ± 0.783 (mean ± std) (mm), 5.613 ± 0.684, 1.383 ± 0.164, 1.267 ± 0.241, 2.725 ± 0.778, and 3.036 ± 0.650, respectively. Comparatively, they were 4.872 ± 0.716, 5.686 ± 0.717, 1.151 ± 0.249, 1.280 ± 0.275, 3.033 ± 0.587, and 3.339 ± 0.522 by the radiologist expert, respectively. The scatter plots of these measurements are shown in Figures 4B-G.

The ICC agreement scores were 0.77 [0.71, 0.83] (95% CI), 0.83 [0.77, 0.87], 0.25 [-0.04, 0.48], 0.32 [0.18, 0.44], 0.72 [0.41, 0.85], and 0.73 [0.28, 0.87], respectively. Only the AP's 95% CI was in the moderate reliability (agreement) range and Trans' 95% confidence interval was in the good reliability range. Rest of the ICC scores were considered poor reliability. While comparing the AI-detected inner wall boundaries with those by PLM, LAP and LTrans measurements (Figs. 4H and 4I) had excellent and good ICC scores of 0.98 [0.97, 0.99] and 0.95 [0.80, 0.98] respectively. All the morphological measurements and ICC scores are summarized

in Table 1.

BA luminal diameters

The fine-tuned Detectron2 model was applied to estimate the proximal, mid, and distal BA diameters (D_{prox}, D_{mid}, and D_{dist}) from all 36 datasets using the proposed centerline resampling strategy. It has successfully detected 35 (97.2 %) datasets. The failed dataset had poor conspicuity in its distal segment. Figure 6 presents the distribution and comparison of BA luminal diameters from 35 datasets. The means of D_{prox}, D_{mid}, and D_{dist} were 3.170 ± 0.685, 2.840 ± 0.629, and 2.712 ± 0.554 mm, respectively. In Figure 6A, the box plot on the left shows that the mean proximal BA diameter (D_{prox}) is the largest compared to the mid and distal BA diameters (D_{mid} and D_{dist}). Student's t-test confirmed that D_{prox} was significantly larger than both D_{mid} and D_{dist} ($p < 0.001$ for both comparisons). The estimated D_{mid} was slightly larger than the estimated D_{dist} ($p = 0.026$). The scatter plot in Figure 6B shows that D_{mid} measurements are generally smaller than the D_{prox}. Similarly, D_{dist} and D_{prox} measurements show a similar pattern in Figure 6C. Figure 6 highlights how the BA diameter changes gradually from the proximal, mid to distal segments. BA luminal diameter and wall thickness measurements are summarized in Tables 2 and 3, respectively. They are compared to the results from previous related

studies [32-39].

Visualization of BA morphological measurements

Figure 7 presents two examples illustrating the BA morphological measurements using our proposed approach. A normal and an atherosclerotic BA example are shown in Figures 7A-D and 7E-H, respectively. Figures 7A and 7B depict the normal BA case's MR scan in lumen-centered coronal and sagittal views, respectively. Figure 7C illustrates the arterial wall thickness estimates at the 12, 3, 6, and 9 o'clock positions respectively. The details of arterial wall thickness and luminal diameter measurements along the BA are illustrated in Figure 7D. It demonstrates that its luminal diameter gradually decreases while its wall thickness remains constant at various slice locations from the proximal to the distal end. Figures 7E-H illustrate the atherosclerotic case with arrows pointing to bright MR spots in Figures 7E and 7F. The diagram in Figure 7H shows a bulged wall thickness curve and a narrowed lumen between slices 40 and 44. Figure 7H also shows that the distal luminal diameter is slightly larger than the proximal luminal diameter, which is atypical compared with common BA cases.

Discussion

Our results indicate that Detectron2, a deep learning segmentation model fine-

tuned through transfer learning with a small dataset of 1073 annotated MR-VWI images, can effectively identify ring-shaped vessel walls. Measurements of outer BA boundary diameters, made by the fine-tuned model, were reliable and showed moderate to good agreement with human expert ratings, with the 95% CI of ICC scores ranging from 0.71 to 0.87. The inner luminal diameters measured by PLM and the trained Detectron2 model showed good to excellent agreement, with the 95% CI of ICC scores ranging from 0.80 to 0.99. Since PLM markings were the de facto ground truth in the training phase, the good ICC scores obtained on unforeseen datasets suggest that deep learning models are consistent and have the potential to automate the detection of BA stenosis from MR-VWI scans.

Wall thickness measurements, on the other hand, showed poor agreement with human expert ratings (ICC < 0.5). The normal BA wall thickness is 0.2–0.3 mm [7], which is smaller than our 1-mm MR-VWI protocol's imaging resolutions (1 mm slice thickness, spatial resolution = 0.2246 or 0.5188 mm) using 3T-MRI. The resultant wall thickness estimates in our study were 1.2 mm by human experts and 1.3 mm by the trained model, indicating that partial volume effects might play a noticeable role limiting the 1 mm MR-VWI's capacity for quantitatively interpreting atherosclerotic plaques. The situation of overestimation has been reported in other

studies [34,35] with estimated values of 0.9–1.0 mm using 3T-MRI. The measurements improve to 0.5–0.6 mm using 7T-MRI with a resolution of 0.13×0.13×0.13 or $0.11\times0.11\times0.11 mm^3$ [36]. In addition, our AI models tended to give relatively low wall thickness estimates for the BA close to the pons, where the outer wall boundaries were not clear (Figs 7C and 7G). Another known obstacle was small arterial branching, making it difficult for the machine to accurately define the boundaries (Fig 5).

Although the resolution of our 1-mm MR-VWI scanning protocol may not be sufficient for quantitative estimation of BA wall thickness, Figures 7E-H demonstrate that the proposed centerline resampling approach can effectively visualize brightened MR intensity spots and bulging wall thickness. With increasing age and atherosclerotic risk factors, extracranial vasa vasorum may extend into the proximal intracranial segments and the vessel walls of the BA, causing similar MR intensity enhancement [40]. Figures 7G and 7H show enlarged distal luminal diameters of the same BA, making the misinterpretation of atherosclerosis less likely. The rationale for this reasoning is that our results support the notion that most BAs exhibit a tapered shape, becoming narrower distally. The enlarged distal segment in Figure 7H appears to remodel itself to compensate for the constricted

mid-segment.

A primary limitation of this study is the absence of a true gold standard for definitively confirming the existence of atherosclerotic plaques. Since the risks associated with performing angiography to diagnose BA stenosis often outweigh the potential benefits, we suggest that follow-up 1-mm MR-VWI or higher-resolution scanning of suspicious lesions as a reasonable, non-invasive alternative for confirmation. A secondary limitation stems from the homogenous nature of the subject pool, which consisted solely of Han Chinese individuals. Finally, the relatively small sample size (20 patients for training, 6 for validation, and 10 for visual scoring) and single-center design may limit the generalizability and reproducibility of the proposed deep learning framework. Consequently, the present results should be interpreted as a feasibility and proof-of-concept demonstration; future multi-center studies with larger cohorts are warranted for further validation.

To facilitate integration of this research into routine clinical practice, future studies will focus on fully automating BA centerline detection and all associated morphological computations. This would make the framework adaptable for investigating the prevalence and morphology of the tapering BA phenotype across

diverse populations, while extending its utility to the detection and characterization of other complex lesions, such as small, blister-like, or perforator-related aneurysms. These lesions are often minute and located at the origins of BA branches, making them difficult to visualize on standard MRA. While this study provides novel insights into BA lumen diameter and wall thickness estimation, it simultaneously underscores the critical need for implementing AI-assisted automation in vessel segmentation to streamline and scale intracranial atherosclerotic studies using MR-VWI throughout the entire cerebrovascular system.

Conclusion

Our study demonstrates the effectiveness of using a 1-mm MR-VWI protocol to characterize BA morphology. Knowledge of the normal tapering of the BA lumen will significantly aid neurosurgeons, neuroradiologists, and neurologists in evaluating and managing posterior circulation vascular diseases, thereby ensuring the safety of periprocedural planning. Furthermore, if our findings regarding abnormal BA remodeling are clinically confirmed, they could lead to non-invasive, alternative methods for monitoring posterior circulation atherosclerotic diseases, utilizing anomalous luminal diameters at different segments as measured by 1-mm

MR-VWI scans.

Acknowledgements

Chien-Hung Tsou and Hon-Man Liu were supported by the intramural research program of Fu Jen Catholic University Hospital.

Funding

This study received no external funding.

References

1 Markus, H. S., van der Worp, H. B. & Rothwell, P. M. Posterior circulation ischaemic stroke and transient ischaemic attack: Diagnosis, investigation, and secondary prevention. *Lancet Neurol* **12**, 989–998, doi:10.1016/s1474-4422(13)70211-4 (2013).

2 Searls, D. E., Pazdera, L., Korbel, E., Vysata, O. & Caplan, L. R. Symptoms and signs of posterior circulation ischemia in the new england medical center posterior circulation registry. *Arch Neurol* **69**, 346–351, doi:10.1001/archneurol.2011.2083 (2012).

3 Sługocki, M. *et al.* Endovascular structures of the basilar artery as forms of the basilar nonfusion spectrum. *Scientific Reports* **15**, 28192, doi:10.1038/s41598-025-14558-z (2025).

4 Reinemeyer, N. E., Tadi, P. & Lui, F. in *Statpearls* (StatPearls Publishing Copyright © 2022, StatPearls Publishing LLC., 2022).

5 Ngo, M. T., Kwak, H. S. & Chung, G. H. Change in basilar artery length and bending according to aging and vertebral artery dominance: A longitudinal study. *Scientific Reports* **10**, 8904, doi:10.1038/s41598-020-65682-x (2020).

6 Kim, J. S. & Caplan, L. R. in *Stroke (seventh edition)* (eds James C. Grotta *et al.*) 368–403.e367 (Elsevier, 2022).

7 Gutierrez, J. *et al.* The contribution of hiv infection to intracranial arterial remodeling: A pilot study. *Neuropathology* **33**, 256–263, doi:10.1111/j.1440-1789.2012.01358.x (2013).

8 Pico, F., Labreuche, J., Gourfinkel-An, I., Amarenco, P. & Investigators, G. Basilar artery diameter and 5-year mortality in patients with stroke. *Stroke* **37**, 2342–2347, doi:10.1161/01.STR.0000236058.57880.03 (2006).

9 Sługocki, M. *et al.* Endovascular structures of the basilar artery as forms of the basilar nonfusion spectrum. *Scientific Reports* **15**, 28192, doi:10.1038/s41598-025-14558-z (2025).

10 Dodevski, A., Lazareska, M., Tosovska-Lazarova, D., Zhivadinovik, J. & Stojkoski, A. Basilar artery fenestration. *Folia Morphologica* **70**, 80–83 (2011).

11 Iqbal, S. A comprehensive study of the anatomical variations of the circle of willis in adult human brains. *J Clin Diagn Res* **7**, 2423–2427, doi:10.7860/jcdr/2013/6580.3563 (2013).

12 Passero, S. G. & Rossi, S. Natural history of vertebrobasilar dolichoectasia.

Neurology **70**, 66–72, doi:10.1212/01.wnl.0000286947.89193.f3 (2008).

13 Koh, W. *et al.* Transcranial doppler sonography is not a valid diagnostic tool for detection of basilar artery stenosis or in-stent restenosis: A retrospective diagnostic study. *BMC Neurol* **17**, 89, doi:10.1186/s12883-017-0872-8 (2017).

14 Zhu, X.-J., Wang, W. & Liu, Z.-J. High-resolution magnetic resonance vessel wall imaging for intracranial arterial stenosis. *Chinese Medical Journal* **129**, doi:10.4103/0366-6999.182826 (2016).

15 Bash, S. *et al.* Intracranial vascular stenosis and occlusive disease: Evaluation with ct angiography, mr angiography, and digital subtraction angiography. *AJNR Am J Neuroradiol* **26**, 1012–1021 (2005).

16 Mossa-Basha, M., Alexander, M., Gaddikeri, S., Yuan, C. & Gandhi, D. Vessel wall imaging for intracranial vascular disease evaluation. *J Neurointerv Surg* **8**, 1154–1159, doi:10.1136/neurintsurg-2015-012127 (2016).

17 Qiao, Y. *et al.* Intracranial arterial wall imaging using three-dimensional high isotropic resolution black blood mri at 3.0 tesla. *J Magn Reson Imaging* **34**, 22–30, doi:10.1002/jmri.22592 (2011).

18 Dieuwertje, A., Christoph, B. & Jelmer, M. W. in *Proc.SPIE.* 120320Y.

19 Alblas, D., Brune, C. & Wolterink, J. M. in *Medical Imaging 2022: Image Processing.* 237–244 (SPIE).

20 Yu, J. *et al.* Plaque distribution of low-grade basilar artery atherosclerosis and its clinical relevance. *BMC neurology* **17**, 8 (2017).

21 van't Klooster, R. *et al.* Automatic lumen and outer wall segmentation of the carotid artery using deformable three-dimensional models in mr angiography and vessel wall images. *Journal of Magnetic Resonance Imaging* **35**, 156–165 (2012).

22 Zhou, H., Xiao, J., Fan, Z. & Ruan, D. in *2021 IEEE 18th International Symposium on Biomedical Imaging (ISBI).* 1416–1419 (IEEE).

23 Isensee, F., Jaeger, P. F., Kohl, S. A., Petersen, J. & Maier-Hein, K. H. Nnu-net: A self-configuring method for deep learning-based biomedical image segmentation. *Nature methods* **18**, 203–211 (2021).

24 Wasserthal, J. *et al.* Totalsegmentator: Robust segmentation of 104 anatomic structures in ct images. *Radiology: Artificial Intelligence* **5**, e230024 (2023).

25 Cesario, M. *et al.* Automated segmentation of thoracic aortic lumen and vessel wall on 3d bright-and black-blood mri using nnu-net. *Journal of Cardiovascular Magnetic Resonance* (2025).

26 Tsou, C. H., Chang, W. C., Liu, H. M. & Huang, A. in *2024 46th Annual*

International Conference of the IEEE Engineering in Medicine and Biology Society (EMBC). 1–4.

27 Huang, A., Lee, C.-W. & Liu, H.-M. Time to peak and full width at half maximum in mr perfusion: Valuable indicators for monitoring moyamoya patients after revascularization. *Scientific Reports* **11**, 479, doi:10.1038/s41598-020-80036-3 (2021).

28 He, K., Gkioxari, G., Dollár, P. & Girshick, R. in *2017 IEEE International Conference on Computer Vision (ICCV).* 2980–2988.

29 Lin, T.-Y. *et al.* in *Computer Vision – ECCV 2014.* (eds David Fleet, Tomas Pajdla, Bernt Schiele, & Tinne Tuytelaars) 740–755 (Springer International Publishing).

30 Mani, V. *et al.* Carotid black blood mri burden of atherosclerotic disease assessment correlates with ultrasound intima-media thickness. *J Cardiovasc Magn Reson* **8**, 529–534, doi:10.1080/10976640600675245 (2006).

31 Koo, T. K. & Li, M. Y. A guideline of selecting and reporting intraclass correlation coefficients for reliability research. *J Chiropr Med* **15**, 155–163, doi:10.1016/j.jcm.2016.02.012 (2016).

32 Pai, B. S. *et al.* Microsurgical anatomy of the posterior circulation. *Neurol India* **55**, 31–41, doi:10.4103/0028-3886.30424 (2007).

33 Tanaka, M. *et al.* Basilar artery diameter is an independent predictor of incident cardiovascular events. *Arterioscler Thromb Vasc Biol* **33**, 2240–2244, doi:10.1161/ATVBAHA.113.301467 (2013).

34 Zhang, D. P. *et al.* Basilar artery bending length, vascular risk factors, and pontine infarction. *J Neurol Sci* **338**, 142–147, doi:10.1016/j.jns.2013.12.037 (2014).

35 Gunnal, S., Farooqui, M. & Wabale, R. Anatomical variability in the termination of the basilar artery in the human cadaveric brain. *Turk Neurosurg* **25**, 586–594, doi:10.5137/1019-5149.Jtn.12812-14.0 (2015).

36 Satapathy, B. C. & Mohapatra, C. Morphometric study of basilar artery in the eastern indian population. *Asian J Neurosurg* **13**, 689–692, doi:10.4103/ajns.AJNS_321_16 (2018).

37 Harteveld, A. A. *et al.* Data on vessel wall thickness measurements of intracranial arteries derived from human circle of willis specimens. *Data Brief* **19**, 6–12, doi:10.1016/j.dib.2018.04.116 (2018).

38 Cogswell, P. M., Lants, S. K., Davis, L. T. & Donahue, M. J. Vessel wall and lumen characteristics with age in healthy participants using 3t intracranial vessel wall magnetic resonance imaging. *J Magn Reson Imaging* **50**, 1452–1460,

doi:10.1002/jmri.26750 (2019).

39 Cogswell, P. M. *et al.* Vessel wall and lumen features in north american moyamoya patients. *Clin Neuroradiol* **30**, 545–552, doi:10.1007/s00062-019-00819-8 (2020).

40 Mandell, D. M. *et al.* Intracranial vessel wall mri: Principles and expert consensus recommendations of the american society of neuroradiology. *AJNR Am J Neuroradiol* **38**, 218–229, doi:10.3174/ajnr.A4893 (2017).

Table 1. BA morphological measurements in the 10 hold-out datasets using axial view images

Morphological metric	Visual (mm)	*AI (mm)	PLM (mm)	Visual/*AI ICC [95%CI]	PLM/*AI ICC [95%CI]
AP	4.872 ± 0.716	4.963 ± 0.783	-	0.774 [0.71, 0.83]	-
Trans	5.686 ± 0.717	5.613 ± 0.684	-	0.827 [0.77, 0.87]	-
AAP	1.151 ± 0.249	1.383 ± 0.164	-	0.251 [-0.04, 0.48]	-
Rtrans	1.280 ± 0.275	1.267 ± 0.241	-	0.319 [0.18, 0.44]	-
LAP	3.033 ± 0.587	2.725 ± 0.778	2.672 ± 0.840	0.722 [0.41, 0.85]	0.982 [0.97, 0.99]
Ltrans	3.339 ± 0.522	3.036 ± 0.650	2.902 ± 0.700	0.730 [0.28, 0.87]	0.954 [0.80, 0.98]

*Fine-tuned Detectron2 model

AP = Anteroposterior, Trans: Transverse, LAP = Luminal anteroposterior, LTrans = Luminal transverse, AAP = Anterior wall length, RTrans = Right Transverse

Table 2. Comparison of BA luminal diameter measurements with previous studies

Study	Year	Sources	Specimen number	Image / measurement Modality	BA luminal diameter (mm)				
					Range	Mean	Proximal	Mid	Distal
Pai et al. [32]	2007	Cadaver	25	Optical Microscopy	3 - 7	4.3	-	-	-
Gutierrez et al. [7]	2013	Cadaver	12	Optical Microscopy	-	3.2 ± 0.6	-	-	-
Tanaka et al. [33]	2013	Patient	493	MRI, MRA	1.1 - 5.2	2.73 ± 0.70	-	-	-
Zhang et al. [34]	2014	Patient	38	MRA	-	3.82 ± 0.47	-	-	-
Gunnal S. et al. [35]	2015	Cadaver	170	Digital Photography	3 - 6	4.8 ± 0.7	-	-	-
Satapathy et al. [36]	2018	Cadaver	38	Vernier Caliper	2 - 3.9	3.05 ± 0.41	-	-	-
Cogswell et al. [38]	2019	Patient	82	3T-MRI#	-	2.82 ± 0.47	-	-	-
Cogswell et al. [39]	2020	Healthy control	23	3T-MRI#	-	2.82 ± 0.46	-	-	-
Present study									
Manual (axial view)	2024	Patient	10	3T-MRI&	2 - 4.86	3.18 ± 0.58	3.28 ± 0.51	3.17 ± 0.62	3.08 ± 0.58
PLM (axial view)	2024	Patient	10	3T-MRI&	1.3 - 5.2	2.79 ± 0.78	3.01 ± 0.79	2.78 ± 0.74	2.56 ± 0.76

AI (axial view)	2024	Patient	10	3T-MRI[&]	1.4 - 5.1	2.88 ± 0.73	3.08 ± 0.74	2.88 ± 0.70	2.68 ± 0.71
AI (resampling)	2024	Patient	35	3T-MRI[&]	1.48 - 4.6	2.91 ± 0.65	3.17 ± 0.69	2.84 ± 0.63	2.71 ± 0.55

*Resolution 0.13×0.13×0.13 or 0.11×0.11×0.11 mm^3

[#]Slice thickness = 1 mm, spatial resolution = 0.5 mm

[&] Slice thickness = 1 mm, spatial resolution = 0.2246 or 0.5188 mm

Table 3. Comparison of BA wall thickness measurements with previous studies

Study	Year	Sources	Specimen Number	Imaging / measurement modality	BA Wall thickness (mm)			
					Mean	Proximal	Mid	Distal
Gutierrez et al. [7]	2013	Cadaver	12	Optical Microscopy	0.29 ± 0.01	-	-	-
Harteveld et al. [37]	2018	Cadaver	15	7T-MRI*	-	0.61 ± 0.16	-	0.53 ± 0.08
Cogswell et al. [38]	2019	Patient	82	3T-MRI#	0.91 ± 0.10	-	-	-
Cogswell et al. [39]	2020	Healthy control	23	3T-MRI#	0.99 ± 0.12	-	-	-
Present study Manual (axial view)	2024	Patient	10	3T-MRI&	1.21 ± 0.27	1.24 ± 0.28	1.20 ± 0.26	1.20 ± 0.28
AI (axial view)	2024	Patient	10	3T-MRI&	1.33 ± 0.21	1.34 ± 0.22	1.33 ± 0.21	1.31 ± 0.21

*Resolution 0.13×0.13×0.13 or 0.11×0.11×0.11 mm^3

#Slice thickness = 1 mm, spatial resolution = 0.5 mm

&Slice thickness = 1 mm, spatial resolution = 0.2246 or 0.5188 mm

Figure captions

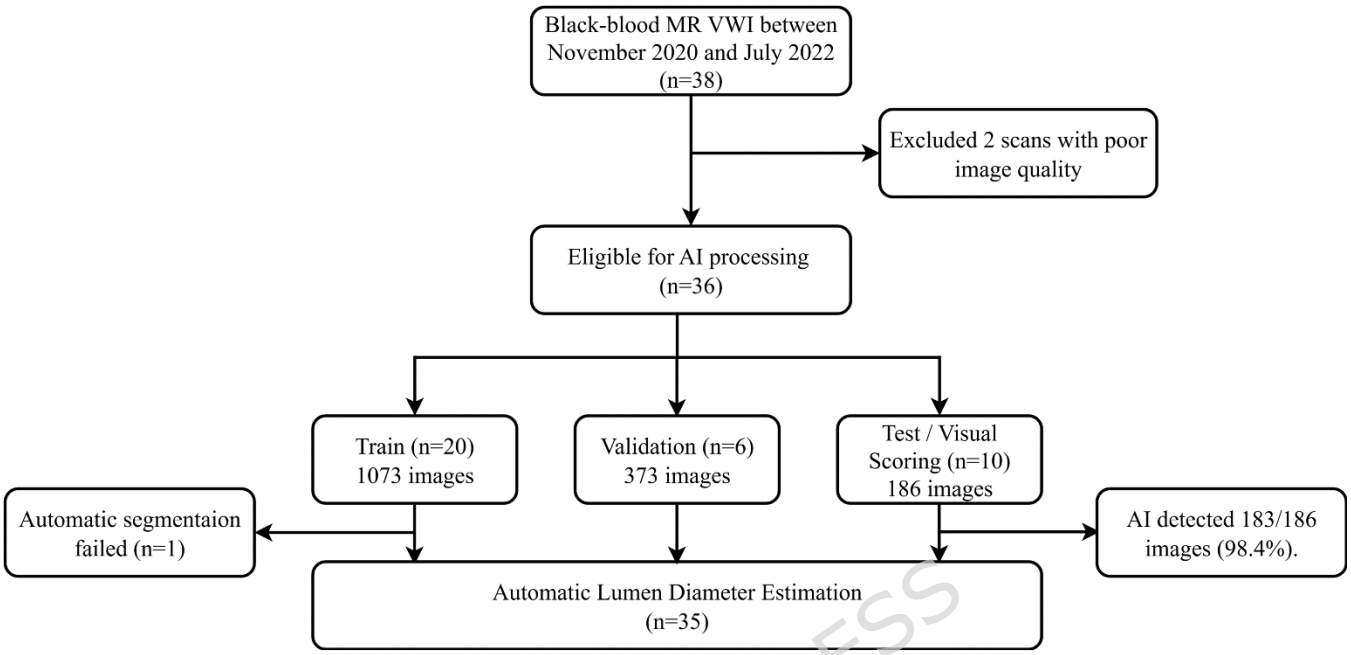

Fig. 1. Flowchart of case inclusion and data splitting for the supervised learning.

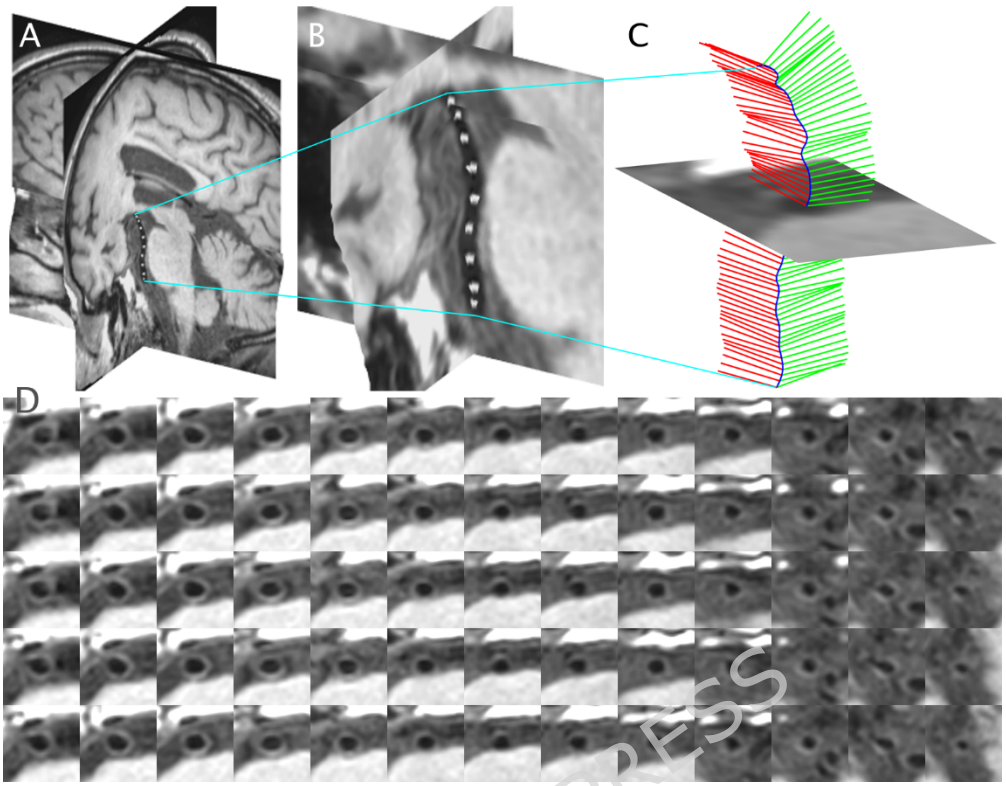

Fig. 2. Steps of the proposed centerline-based resampling strategy.

(A) Manually place BA lumen center points. (B) Zoomed-in view of the BA. (C) Cross-sectional images in the local coordinate system along the BA centerline. (D) Rearrange cross-sectional images from the proximal to the distal BA (in an up-down, left-right order).

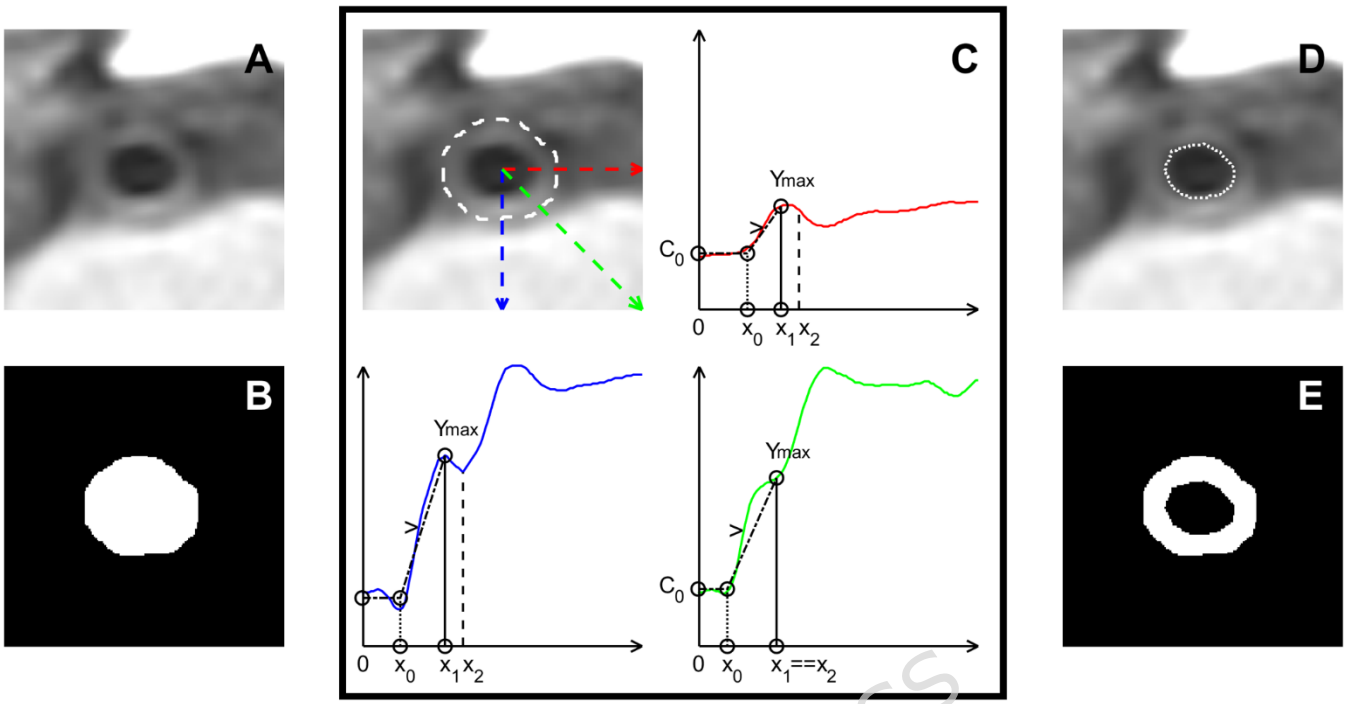

Fig. 3. Automated PLM inner wall annotation algorithm.

(A) Cross-sectional vessel image and (B) its outer wall mask are used as input. (C) Radial samples are drawn and fitted with a PLM to identify the average lumen intensity (C_0), the peak wall intensity (Y_{max}), and their corresponding locations (x_0 and x_1). (D) The inner wall (dotted line) is located at the mid-intensity between the lumen and wall peaks. (E) The final output is the ring-shaped vessel wall mask.

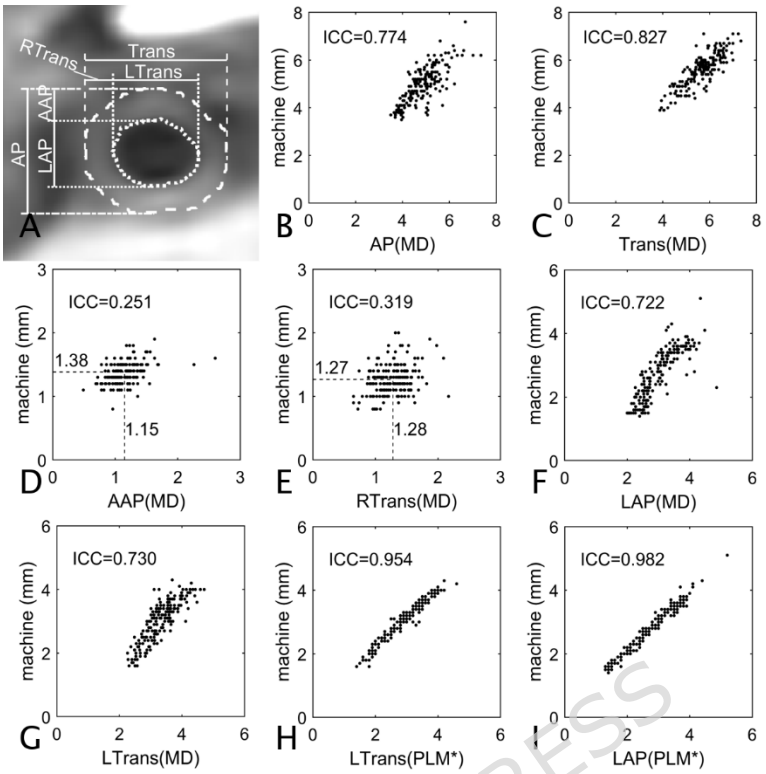

Fig. 4. BA morphology definitions and the levels of agreement with radiologist's measure.

(A) Protocol for manual delineation of BA morphology. (B)-(G) Scatter plots comparing measurements by a human expert (x-axis) and a fine-tuned Detectron2 model (y-axis) for anteroposterior diameter (AP), transverse diameter (Trans), wall thickness at 12 o'clock (AAP), wall thickness at 9 o'clock (RTrans), luminal transverse diameter (LTrans), and luminal anteroposterior diameter (LAP), respectively. (H) and (I) Scatter plots comparing measurements by PLM (x-axis) and the fine-tuned Detectron2 model (y-axis).

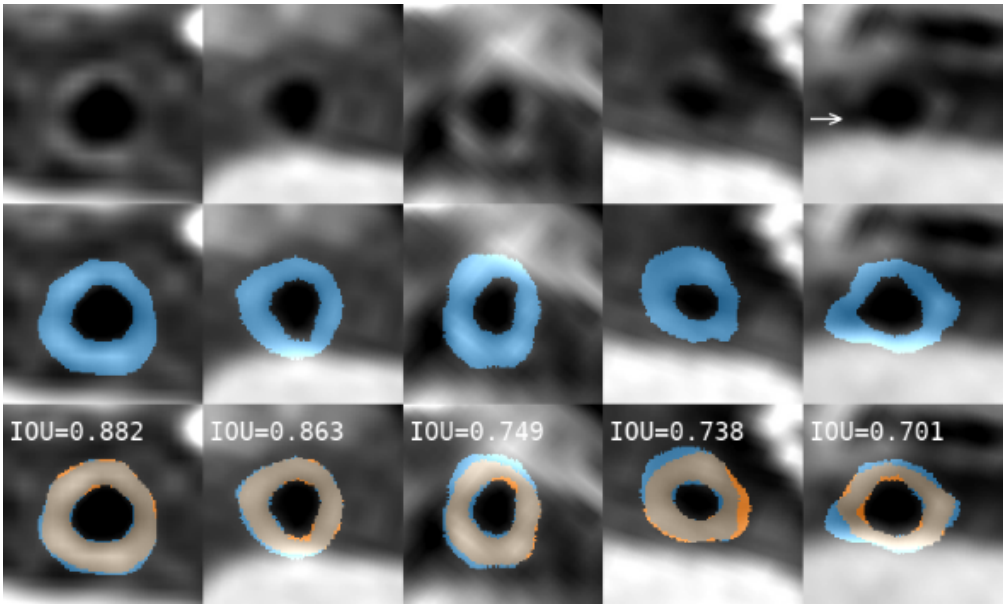

Fig. 5. Automated BA wall segmentation results compared with manual annotations.

Predicted ring-shaped walls by the fine-tuned Detectron2 model are shown in blue (second row), manual annotations in orange (third row), with IOU scores. The arrow in the fifth column indicates a bifurcating branch causing bulging in the prediction.

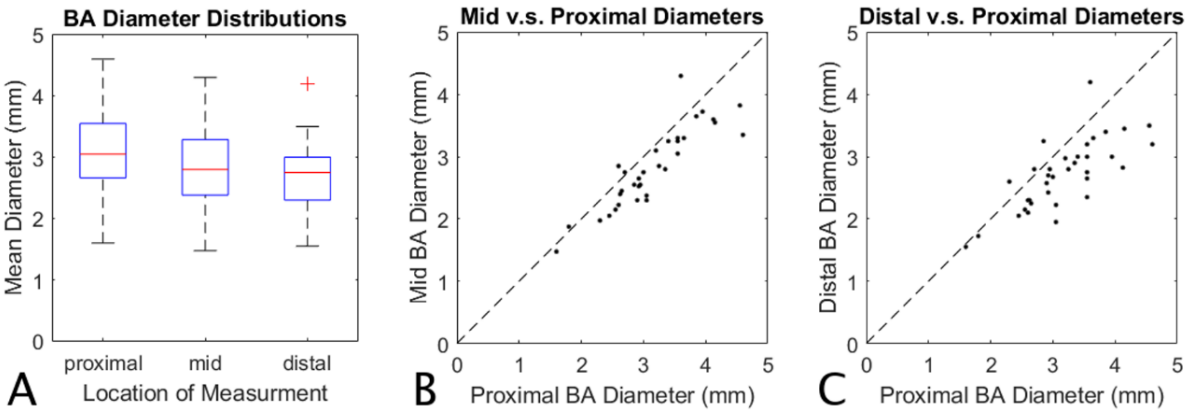

Fig. 6. Statistical distribution of BA lumen diameters at different segments.

(A) Boxplots illustrate the distribution of BA lumen diameters at the proximal, mid, and distal segments (n=35). (B) and (C) Scatter plots compare the diameters of the mid vs. proximal and distal vs. proximal segments, respectively.

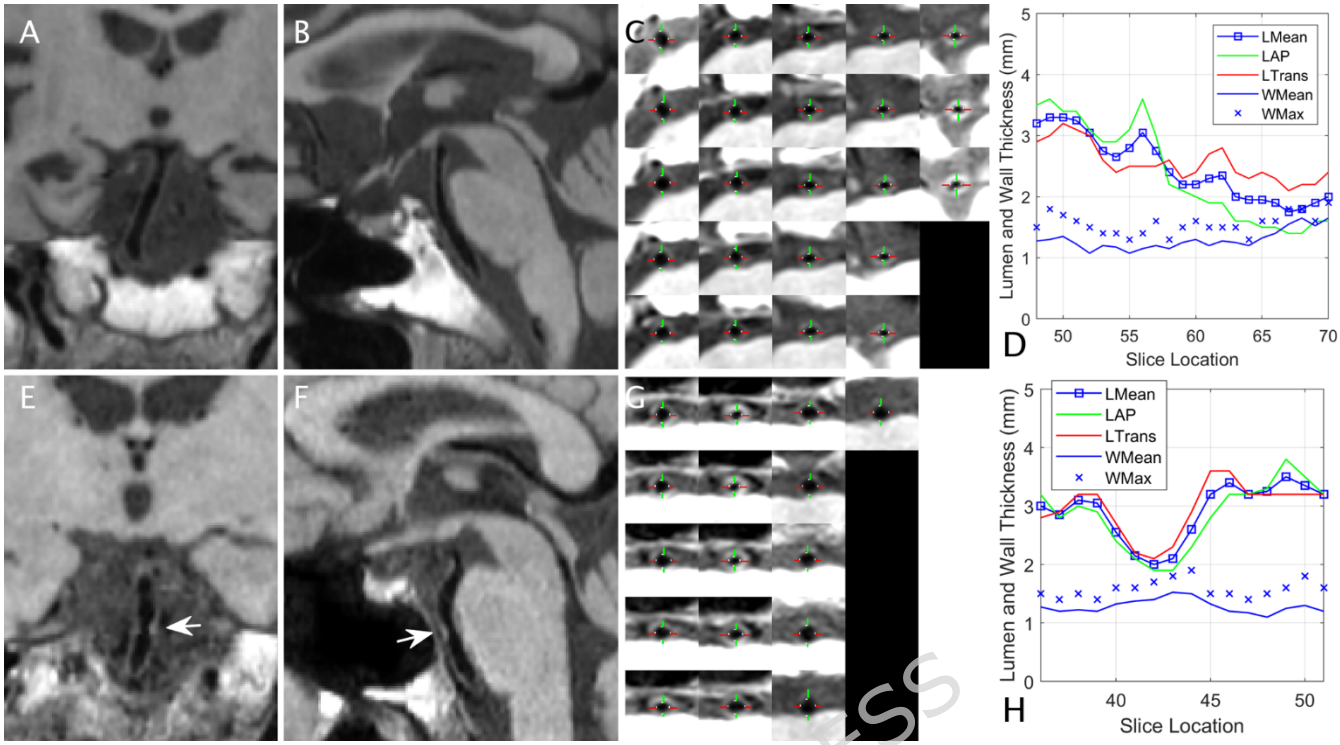

Fig. 7. Typical and atypical cases of BA morphology.

(A-D) A typical, normal case showing lumen diameter and wall thickness profiles across slice locations. (E–H) An atypical case with arrows indicating suspected plaque. LMean, WMean, and WMax represent mean luminal diameter, mean wall thickness, and maximal wall thickness, respectively.